COALESCENCE-INDUCED NANODROPLET JUMPING

BY

HYEONGYUN CHA

THESIS

Submitted in partial fulfillment of the requirements
for the degree of Master of Science in Mechanical Engineering
in the Graduate College of the
University of Illinois at Urbana-Champaign, 2016

Urbana, Illinois

Adviser:

Assistant Professor Nenad Miljkovic

ABSTRACT

Water vapor condensation on superhydrophobic surfaces has received much attention in recent years due to the ability of such surfaces to shed microscale water droplets via coalescence-induced droplet jumping, resulting in heat transfer, anti-icing, and self-cleaning performance enhancement. Here, we report for the first time the coalescence-induced removal of water nanodroplets ($R \approx 500$ nm) from superhydrophobic carbon nanotube (CNT) surfaces. The two-droplet coalescence time is measured for varying droplet Ohnesorge numbers, confirming that coalescence prior to jumping is governed by capillary-inertial dynamics. By varying the conformal hydrophobic coating thickness on the CNT surface, the minimum jumping droplet radius was shown to increase with increasing solid fraction and decreasing apparent advancing contact angle, indicating that hydrodynamic limitations stemming from viscous dissipation do not limit the minimum droplet jumping size even for the smallest nanostructure length scale ($\leq$ 100 nm) and surface adhesion. Rather, a surface interaction mechanism stemming from the evolved droplet morphology plays the defining role in limiting the minimum size for jumping. The outcomes of this work demonstrate the ability to passively shed nanometric water droplets, which has the potential to further increase the efficiency of systems that can harness jumping droplets for a wide range of energy and water applications.

To my parents

Incheon Cha and Jeonghui Kim

and

To my brother

Hyeongjip Cha

ACKNOWLEDGEMENTS

I would like to express sincere thanks to my thesis supervisor, Professor Nenad Miljkovic, for his advice, patience, and professional guidance throughout my studies. Professor Miljkovic was not only a good research advisor that provided me research directions, but also was a great mentor who allowed me to be a better person. I would also like to thank all of my colleagues in Energy Transport Research Laboratory (ETRL) for helping me to adapt to the research lab environment and for being good friends. I want to express special thanks to my parents, Incheon and Jeonghui. They always supported, motivated, and helped my brother and me to provide us a chance to pursue our dreams. Finally, I gratefully acknowledge the support of the International Institute of Carbon Neutral Energy Research (WPI-I2CNER), sponsored by the Japanese Ministry of Education, Culture, Science and Technology, and the support from the Air Conditioning and Refrigeration Center (ACRC), an NSF-founded I/UCRC at UIUC.

TABLE OF CONTENTS

CHAPTER 1: INTRODUCTION

Water vapor condensation is routinely observed in nature and has a large influence on the performance of industrial systems.[1-5] When water condenses on non-wetting hydrophobic surfaces, it undergoes 'dropwise' condensation[6] with an order of magnitude enhanced heat transfer under pure vapor conditions when compared to condensation on wetting hydrophilic substrates due to the formation of small liquid droplets which grow, shed *via* gravitational body force (≈ 2 mm for water) and, in the process, clear the surface for re-nucleation.[7] More recently, researchers have discovered that microdroplets (~10-100 μm) condensing and coalescing on suitably designed superhydrophobic surfaces can lead to droplets jumping away from the surface irrespective of gravity due to surface-to-kinetic energy transfer.[8-13] This spontaneous droplet removal[14-24] has been utilized for a variety of applications including self-cleaning,[25-27] thermal diodes,[26,28] anti-icing,[29-32] vapor chambers,[33] electrostatic energy harvesting,[34-36] fiber-based coalescers,[37] and condensation heat transfer enhancement.[38-50] The minimum droplet size where coalescence-induced jumping occurs governs the performance of applications exploiting the phenomenon. Removal of the condensate at smaller length scales reduces the thermal transport resistance through the condensate,[40] enhances jumping speeds due to more efficient surface-to-kinetic energy transfer,[9] and allows for the more efficient control of droplet motion with external fields against adverse forces such as gravity or vapor flow.[51] However, the mechanism governing the minimum jumping droplet size is not well understood. Previous studies have reported that below a critical radius of ≈10 μm (at standard laboratory conditions) droplets coalesce, but do not jump due to hydrodynamic limits stemming from internal viscous dissipation during coalescence.[17,49,52-57] Furthermore, at these low radii (R < 10 μm) droplets jump with lower speeds than predicted by inertial-capillary scaling, which matches experiments well at larger

droplet radii. Here, we report water nanodroplet jumping on ultra-low adhesion carbon nanotube (CNT) surfaces. Through theoretical and experimental analysis of two-droplet coalescence timescales during jumping, we show that inertial-capillary dynamics, not viscous effects, govern jumping down to nanodroplet length scales ($R \approx 500$ nm). Previous findings are reconciled by realizing that the combined effects of adhesion, contact angle hysteresis, and initial wetting behavior governed by the surface structure morphology and length-scale, define the minimum droplet departure size and observed speed reduction at low radii.

CHAPTER 2: RESULTS AND DISCUSSION

2.1 Experiments

The growth, coalescence, and jumping of droplets was studied using a custom built top-view optical light microscopy set-up by condensing water vapor either from the ambient, or from a saturated vapor supply on substrates having temperatures T_w = 1 ± 0.5°C. The experimental setup is shown in Fig. (A1) with procedures detailed in the Ref. [9]. A CNT coated silicon wafer was chosen as a model condensation substrate due to the small length scale of the nanotubes (~10 nm), the low solid fraction (φ) of the short nanotubes and, thus, the potential for achieving ultra-low adhesion after hydrophobic functionalization. Carbon nanotubes were grown by chemical vapor deposition (CVD) on silicon.[9] The thermally grown CNTs had a typical outer diameter of $d \approx 7$ nm and formed tangled turf instead of an aligned forest due to the short growth time (≈5 minutes). The characteristic turf height was determined to be $h \approx 1 \pm 0.3$ μm via atomic force microscopy. To functionalize the surfaces, a proprietary fluorinated polymer was deposited using plasma enhanced vapor deposition (P2i) under low pressure at room temperature. This process allows for the development of a highly conformal, but thin (≈10 nm) polymer layer (Fig. 1a, b). Goniometric measurements (MCA-3, Kyowa Interface Science Ltd.) of droplets on a smooth P2i coated silicon wafer showed advancing and receding contact angles of θ_a = 124.3 ± 3.1° and θ_r = 112.6 ± 2.8°, respectively. To quantify the effects of droplet-surface interaction, we also fabricated identical CNT turf samples to the one described above (CNT1), but with varying fluoropolymer thicknesses of ≈30 nm (CNT2, Fig. 1c), 60 nm (CNT3, Fig. 1d), and 90 nm (CNT4, Fig. 1e) to vary the effective solid fraction and, thus, the surface adhesion characteristics. Using the values of the advancing angles on the rough and smooth P2i surfaces, we estimated the solid fraction of the of the 10, 30, 60, and 90 nm CNT surfaces to be $\varphi = (\cos\theta_a^{app} + 1)/(\cos\theta_a + 1)$

≈ 0.017, 0.06, 0.15, and 0.23, respectively. The CNT2, CNT3, and CNT4 samples had an increased effective solid fraction due to the filling of nanoscale gaps between CNTs (Figs. 1c-d), resulting in a reduced apparent contact angle ($\theta_{\mathrm{a}}^{\mathrm{app}}$), increased droplet-surface adhesion and increased contact angle hysteresis. The apparent advancing and receding contact angles ($\theta_{\mathrm{a}}^{\mathrm{app}}/\theta_{\mathrm{r}}^{\mathrm{app}}$) on the CNT1, CNT2, CNT3, and CNT4 surfaces were measured to be ≈ 173º/164°, 163º/152°, 159º/146°, and 154º/140°, respectively.

2.2 Minimum Jumping Droplet Size

Droplet nucleation on the CNT surfaces occurred primarily within nanostructures (due to small φ) in a spatially random fashion[58] and, while growing beyond the confines of the structures, the apparent contact angle increased as the droplets developed a balloon-like shape with a liquid bridge at the base.[41,58] On the CNT1 surface, once droplets grew to diameters large enough to coalesce with neighboring droplets ($R \approx 5$ μm for ambient conditions), frequent out-of-plane jumping was observed. Due to the high conformality and low defect density of the P2i coating, condensation experiments in ambient conditions with $T_{\mathrm{air}} = 22 \pm 0.5$°C and relative humidity $\Phi = 28 \pm 1\%$ resulted in nucleation densities of $N \leq 2.5$ x 10^9 droplets/m^2. In order to study the behavior of interacting *nanoscale* droplets, the nucleation density on the CNT1 surface was elevated by increasing the saturation temperature of the incoming vapor supply to $T_{\mathrm{air}} = 35 \pm 0.5$°C and relative humidity $\Phi \approx 100 \pm 1\%$. The increased saturation temperature resulted in a supersaturation ($S = [\Phi P_{\mathrm{sat}}(T_{\mathrm{air}})]/P_{\mathrm{sat}}(T_{\mathrm{w}})$) increase from $S = 1.02 \pm 0.035$ to $S = 8.56 \pm 0.4$, and a corresponding increase in the nucleation rate and active nucleation site density to $N \geq 1.1$ x 10^{10}, consistent with nucleation site activation.[59] At the elevated nucleation densities, the center-to-center spacing between neighboring droplets was as low as ≈500 nm. Surprisingly, frequent out-of-plane jumping was still observed at these reduced droplet coalescence length scales on the CNT1 surface (Fig. 2), with droplets having radii as small as $R_1 = 533 \pm 75$ nm and $R_2 = 792 \pm 75$ nm coalescing and jumping from the surface (Fig. 2b). In addition to jumping resulting from the coalescence of two nanodroplets (defined as nano based on their radii), serial coalescence between three nanodroplets resulted in jumping as well (Fig. 2c, d). Conservation of mass of the coalescing droplets showed droplet departure radii as small as $R_{\mathrm{j}} = 700 \pm 75$ nm, well below the previously observed limit of $R_{\mathrm{j}} > 5$ μm. It is important to note that the higher supersaturations used

in these experiments (S = 8.56 ± 0.4) did not lead to nucleation-mediated surface flooding, which was shown to occur for S > 1.12 for nanostructured superhydrophobic copper oxide (CuO) surfaces.[50] Increased supersaturations without flooding were achieved as a result of the reduction in structure length scale from $l \approx 1$ μm (CuO) to $l \approx 50$ - 100 nm (CNT1) and the characteristically lower nucleation density on the P2i coating at a given supersaturation. The reduced length scale allowed for the average spacing between randomly distributed nucleation sites ($\langle L \rangle$) to be much smaller while simultaneously allowing individual droplets to form the energetically favorable partially wetting droplet morphology prior to coalescence and jumping ($\langle L \rangle / l \gg 1$).[38,39,50] Furthermore, the nanoscale droplet jumping phenomena was not observed on the CNT2, CNT3, or CNT4 surfaces for ambient or high supersaturation conditions due to increased droplet-surface adhesion (to be discussed later).

2.3 Coalescence Timescale

To explain the jumping of nanoscale droplets observed here, we begin by examining the hydrodynamics of droplet coalescence between two equally sized droplets on the superhydrophobic CNT surfaces. Immediately after the interfaces of the two droplets touch, a radially accelerating liquid bridge develops due to the curvature difference between the bridge radius ($1/r_b$) and the radii of the coalescing droplets ($1/R$). The momentum of this radial flow structure has been shown to drive droplet jumping[22]. For the droplet length scales considered here (500 nm < R < 200 μm), the Ohnesorge number, $\mathrm{Oh} = \mu/(\rho\gamma R)^{1/2}$, where μ (=1.73 mPa·s), ρ (=999.85 kg/m^3), and γ (=75.5 mN/m) are, respectively, the water dynamic viscosity, density, and surface tension, corresponds to 0.26 > Oh > 0.013. For small Oh (Oh < 1), droplet coalescence occurs in two distinct regimes.[60,61] When $r_b/R < \mathrm{Oh}$, droplets undergo coalescence in the inertially-limited viscous regime where growth of the bridge radius is governed by a balance between viscous and surface tension forces, $r_{b,v} = \gamma t/\mu$. As the liquid bridge proceeds to grow, and reaches $r_b/R > \mathrm{Oh}$, the droplets enter the inertially-limited regime where growth of the bridge radius is governed by a balance between inertia and surface tension forces, $r_{b,i} = D_0(\gamma R/\rho)^{1/4}t^{1/2}$, where D_0 is a constant with value ranging between 1.39 and 1.62.[60,62,63] The crossover between these two regimes occurs when the Reynolds number ($\mathrm{Re} = \rho UL/\mu$) based on the neck height ($L = {r_b}^2/2R$) approaches unity ($\mathrm{Re} \approx 1$), corresponding to a critical bridge radius of $r_c \approx 8\mu(R/\rho\gamma {D_0}^4)^{1/2}$.[60] For the smallest droplets coalescing on our CNT surfaces ($R \approx$ 500 nm), r_c = 398 nm based on D_0 = 1.62, which is below the observed minimum jumping radius for CNT1. For larger droplets, the discrepancy is even greater, showing r_c/R = 0.33 for R = 3 μm, and r_c/R = 0.18 for R = 10 μm. The early crossover between the two regimes ($r_c/R \ll 1$) indicates that the coalescence hydrodynamics are governed by inertial-capillary effects, with

viscosity playing a limited role for microscale droplets (R > 1 μm). Indeed, by calculating the viscous-to-inertial crossover time, $\tau_c = 64\mu^2[R/(\rho\gamma^3 {D_0}^{12})]^{1/2}$, and normalizing it to the total coalescence time for the bridge radius to reach the droplet radius ($r_b = R$), $\tau_{tot} = \tau_v + \tau_i = r_c\mu/\gamma + (\rho/\gamma {D_0}^4)^{1/2}(R^{3/2} - {r_c}^{3/2})$, we can estimate the time spent in each regime during coalescence. For droplets having radii R = 0.5, 3, and 10 μm, we obtain τ_c/τ_{tot} = 0.65, 0.1, and 0.029, respectively, indicating that inertial-capillary forces govern droplet coalescence even at nanometric length scales. Therefore, the underlying cause preventing droplet jumping for R > 1 μm at standard laboratory conditions is not viscous dissipation (as put forward in Refs. [17,49,52-57]), but most likely a droplet-surface interaction mechanism arising due to finite surface adhesion and the evolving droplet morphology at length scales comparable to that of the surface structures. Note, the minimum coalescing droplet size reported here ($R \approx$ 556 nm) that leads to jumping agrees well with the theory, as the crossover radius approaches the coalescence radius at these small length scales (r_c = 420 nm). Observations of ultra-small droplets coalescing (R < 500 nm) was difficult to observe due to the resolution limitations of our optical microscopy setup (diffraction limit). However, coalescence without jumping on our CNT1 surface was observed for droplets having sizes as small as $R_1 = R_2$ = 375 ± 300 nm, consistent with our theoretical estimate described below.

To verify that the coalescence hydrodynamics are indeed dominated by inertial effects for the droplet size range discussed above, we experimentally measured the coalescence timescale (τ_{tot}) for a variety of droplet Oh (0.1 > Oh > 0.013, corresponding to 3 μm < R < 200 μm). We were unable to characterize smaller droplets (R < 3 μm) due to the ultra-fast (τ_{tot} < 1 μs) coalescence process at these length scales and the limitation of our high-speed camera to 10^6 frames per second. Individual coalescence events were observed *via* top-down high speed imaging of condensing

water vapor from standard laboratory conditions (Fig. 3a). To measure the coalescence time of both jumping and non-jumping events, we tested the CNT1 and CNT3 samples. While the CNT1 sample showed droplet jumping for all droplet length scales (500 nm < R < 200 μm), many coalescence events on the CNT3 surface resulted in non-jumping due to increased adhesion. Figure 3(b) demonstrates that droplet jumping hydrodynamics on the superhydrophobic CNT surfaces are indeed governed by inertial effects down to the smallest droplet sizes we could measure. The jumping and non-jumping experimental data is in good agreement with the predicted value from the inertial regime ($\tau_{\mathrm{i}} = (R^3\rho/\gamma {D_0}^4)^{1/2}$) and a poor fit with the inertially-limited viscous regime ($\tau_{\mathrm{v}} = R\mu/\gamma$). Furthermore, the experimental data reveals no statistical difference between the coalescence timescale of jumping and non-jumping events. These findings support the view that a surface interaction mechanism rather than a fundamental hydrodynamic limitation governs the minimum droplet jumping size over the range of Oh investigated. Furthermore, the previously reported lower than expected jumping speeds cannot be attributed to viscous effects during coalescence,[17,49,52-57] as the jumping speeds in previous works decrease faster than observed in experiments on similar CNT surfaces shown here in this range of Oh (< 0.1),[9] pointing to a non-hydrodynamic mechanism.[9-11,64]

2.4 Droplet-Surface Interaction

To quantify the effects of droplet-surface interaction, we experimentally observed the condensation behavior on the CNT2, CNT3, and CNT4 surfaces. As $\theta_{\mathrm{a}}^{\mathrm{app}}/\theta_{\mathrm{r}}^{\mathrm{app}}$ decreased from ≈ 173º/164° (CNT1), to 163º/152° (CNT2), 159º/146° (CNT3), and 154º/140° (CNT4), the minimum droplet departure radius increased correspondingly to R_{j} ($\approx 2^{1/3}R$) ≈ 700 nm, 4.5 μm, 20 μm, and no jumping, respectively. The increasing minimum jumping radius can be understood by analyzing the *available* excess surface energy, E_{j}, released during coalescence due to change in liquid/vapor and liquid/solid interfacial area, (see Appendix B, for derivation)

$$E_{\mathrm{j}} \approx \eta\left[\Delta E_{31,\mathrm{lv}} + (W_{31} - W_{32})\right] + W_{32} + W', \tag{1}$$

where η is the conversion efficiency of excess liquid/vapor surface energy to translational kinetic energy,[9,10] $\Delta E_{31,\mathrm{lv}}$ is the contact angle dependent excess liquid/vapor surface energy, $W_{31} - W_{32}$ is the net work of adhesion to be overcome as the system transitions from its initial wetting state to an intermediate state before jumping (Fig. 4a), W_{32} is the work of adhesion to be overcome for the coalesced droplet to depart the condensing surface and W' is an additional adhesion term to account for dynamically wetted surface area in the presence of contact angle hysteresis. Note that, based on our sign convention, droplet jumping is predicted to occur when $E_{\mathrm{j}} < 0$.

In developing a picture of the overall process, the *total* excess surface energy, $\Delta E_{31,\mathrm{lv}}$, released during coalescence is first compared to the net work of adhesion as the droplet coalesces to a single droplet before departing the surface, $W_{31} - W_{32}$ (process between E_1 and E_2 in Fig. 4a). To calculate the *total* excess surface energy $\Delta E_{31,\mathrm{lv}} = f\left(R, \theta_{\mathrm{a}}^{\mathrm{app}}\right)$ available for droplet jumping, we

considered two droplets coalescing with equivalent radii. This excess energy is responsible for generating the internal flow, namely the characteristic bridging flow formed during droplet coalescence.[9,10,12] W_{31} is the surface adhesion associated with the portion of the droplet base residing in the nominal Cassie-Baxter state and the pinned region (r_p) (see Fig. 4a) that is typically formed during the initial nucleation and growth of condensed droplets.[19,41,58] The magnitude of r_p is dictated by the initial wetting interactions of the droplet at the length-scale, l, of the underlying surface structure, *i.e.*, $r_\mathrm{p} \sim l$.[58] W_{32} is the surface adhesion associated with the coalesced droplet on the condensing surface just prior to departure. The difference in energy between W_{31} and W_{32} is overcome by the excess liquid/vapor surface energy while it is simultaneously driving the generation of the bridging flow. In the limit as $R \to r_\mathrm{p}$, $W_{31} \to \Delta E_{31,\mathrm{lv}}$ and insufficient excess energy is available to depin the droplets.[40] As $R \gg r_\mathrm{p}$, W_{31} approaches the limit given by the droplet residing completely in the Cassie-Baxter state.

As the bridging flow develops to the point of impact with the substrate, the droplet will begin developing a net translational acceleration. The *available* excess energy to drive this translational motion is estimated as $\eta\left[\Delta E_{31,lv} + (W_{31} - W_{32})\right]$, where the conversion efficiency, η, captures the fraction of internal flow momentum contributing to the jumping process (process between state E_2 and E_3 in Fig. 4a). Here η is found by defining a cut-off Oh for jumping in the limit of no surface adhesion based on the cross-over from the inertially-limited viscous to inertial bridging regimes, $\mathrm{Oh_c} = D_0^2/8$ and fitting a double exponential with our previous numerical results[9] (see Appendix B, for details). Some of this *available* excess energy is then required to overcome the work of adhesion as the droplet leaves the surface, $W_{32} + W'$.

To compare our experimental observations to the predictions of Eq. (1), we first set $W' = 0$ and define a θ_a^{app} dependent contact angle hysteresis based on a fit to our experimentally measured apparent advancing and receding contact angles for the different surfaces (see Appendix B, for details). Figure 4(b) shows a phase map generated from Eq. (1) with our experimental observations overlaid. When $E_j > 0$, droplet jumping is not possible and the newly formed droplet remains on the surface (orange shaded region in Fig. 4b). However, when $E_j < 0$, sufficient excess surface energy is available for conversion into the kinetic energy for droplet jumping, resulting in successful departure (aquamarine shaded region in Fig. 4b). For comparison, we have also plotted the prediction of Eq. (1) by considering an idealized surface where no hysteresis exists for the Cassie-Baxter state ($\theta_r = \theta_a$). We see that accounting for hysteresis effects is crucial to explaining the observation of no jumping events for our CNT4 surface, whereas for our CNT1 surface, the observed jumping threshold ($R \approx 556$ nm) is primarily dictated by viscous considerations and the pinned base area rather than hysteresis effects since $R(\mathrm{Oh}_c) \approx 369$ nm compared to the calculated R_c, including surface wetting interactions, of 425 nm.

However, for our CNT2 and CNT3 surfaces, we observe a significant discrepancy between the data and our hysteresis model based on equilibrium interfacial areas ($W' = 0$). The comparison between our model and data can be improved by including an additional adhesion term ($W' > 0$). This added adhesion would be present if there is an additional dynamically (non-equilibrium) wetted surface area driven by the inertia of the bridge impacting the surface during coalescence that only contributes to the overall energy balance if the surface is hysteretic. We have assumed that this additional wetted area is proportional to the equilibrium wetted surface area in state E_2 and is Oh dependent, *i.e.*, the dynamically wetted area decreases as Oh increases (inertia

decreases). The dashed curve in Fig. 4(b) shows the predictions of our model including an additional dynamically wetted area that, in the limit of small Oh, is ~10% of the equilibrium wetted surface area in state E_2. Based on this modification, calculations of the jumping threshold ($E_j = 0$) for the four CNT surfaces yielded minimum initial droplet radii for jumping of 425 nm, 2.05 μm, 14.75 μm and no jumping, respectively, in excellent agreement with the experimentally determined values of 530 nm, 3.57 μm, 15.87 μm, and no jumping for $R < 100$ μm. By considering the role of surface adhesion and contact angle hysteresis at different stages of the jumping process in combination with a reasonably bounded viscous dissipation term, we have developed a more refined way of determining the jumping droplet threshold compared to previous estimates.[43,56,65]

2.5 Figures

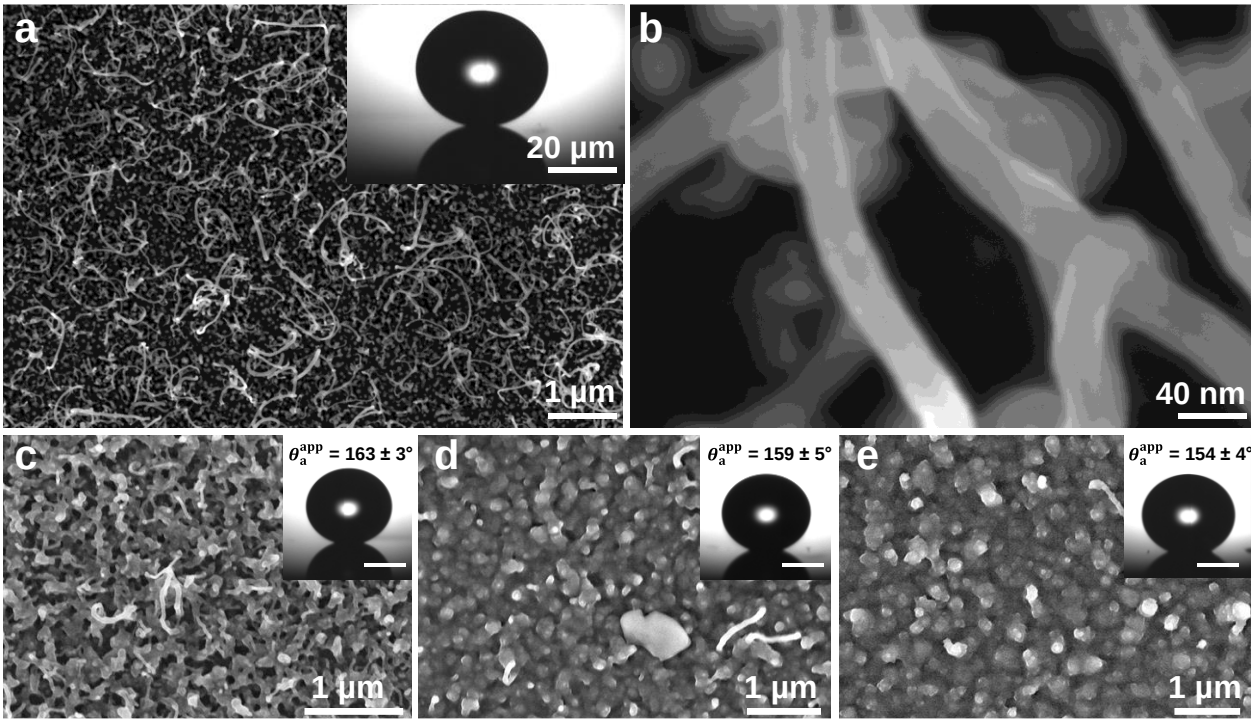

Figure 1. Field emission scanning electron micrographs (Hitachi model S-4800) of (a) a top-down view of the CNT surface coated with a ≈10 nm thick layer of P2i fluoropolymer (CNT1) and (b) a high magnification view of individual CNTs shown in (a). Inset: Microscopic droplet in the receding state on the P2i-coated CNT surface (θ_r^{app} = 164 ± 6°). The CNTs have characteristic diameters $d \approx 7$ nm, heights, $h \approx 1$ µm, and solid fraction, $\varphi \approx 0.017$. Field emission scanning electron micrographs of a top-down view of the (c) CNT2, (d) CNT3, and (e) CNT4 surfaces coated with 30 nm, 60 nm, and 90 nm thick layers of P2i fluoropolymer, respectively. Insets: Microscopic droplets in the advancing state on the P2i-coated CNT surfaces. Inset scale bars are 20 µm each. The effective solid fraction of the CNT surfaces shown in (c), (d), and (e) are estimated as $\varphi \approx 0.06$, 0.15, and 0.23, respectively.

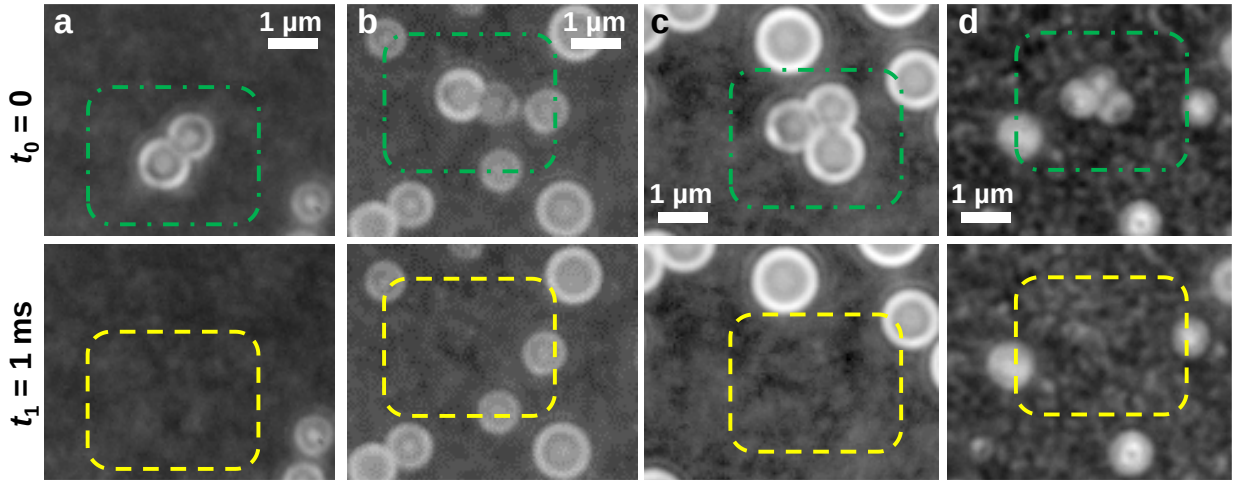

Figure 2. Time-lapse images captured via top-view optical microscopy of steady state water condensation on the superhydrophobic CNT1 surface. Condensing nanoscale droplets having (a) R_1 = 685 ± 75 nm (bottom) and R_2 = 640 ± 75 nm (top), (b) R_1 = 792 ± 75 nm (left) and R_2 = 533 ± 75 nm (right), (c) R_1 = 762 ± 75 nm, R_2 = 716 ± 75 nm, and R_3 = 792 ± 75 nm, and (d) R_1 = 727 ± 75 nm, R_2 = 681 ± 75 nm, and R_3 = 568 ± 75 nm, underwent spontaneous jumping after coalescence. Green dot-dash squares highlight areas of the surface just prior to coalescence, while yellow dashed squares highlight areas of the surface immediately after jumping (1 ms later). High speed imaging was done at 1,000 frames/s, with an exposure time of 200 µs, and a period of 1 ms.

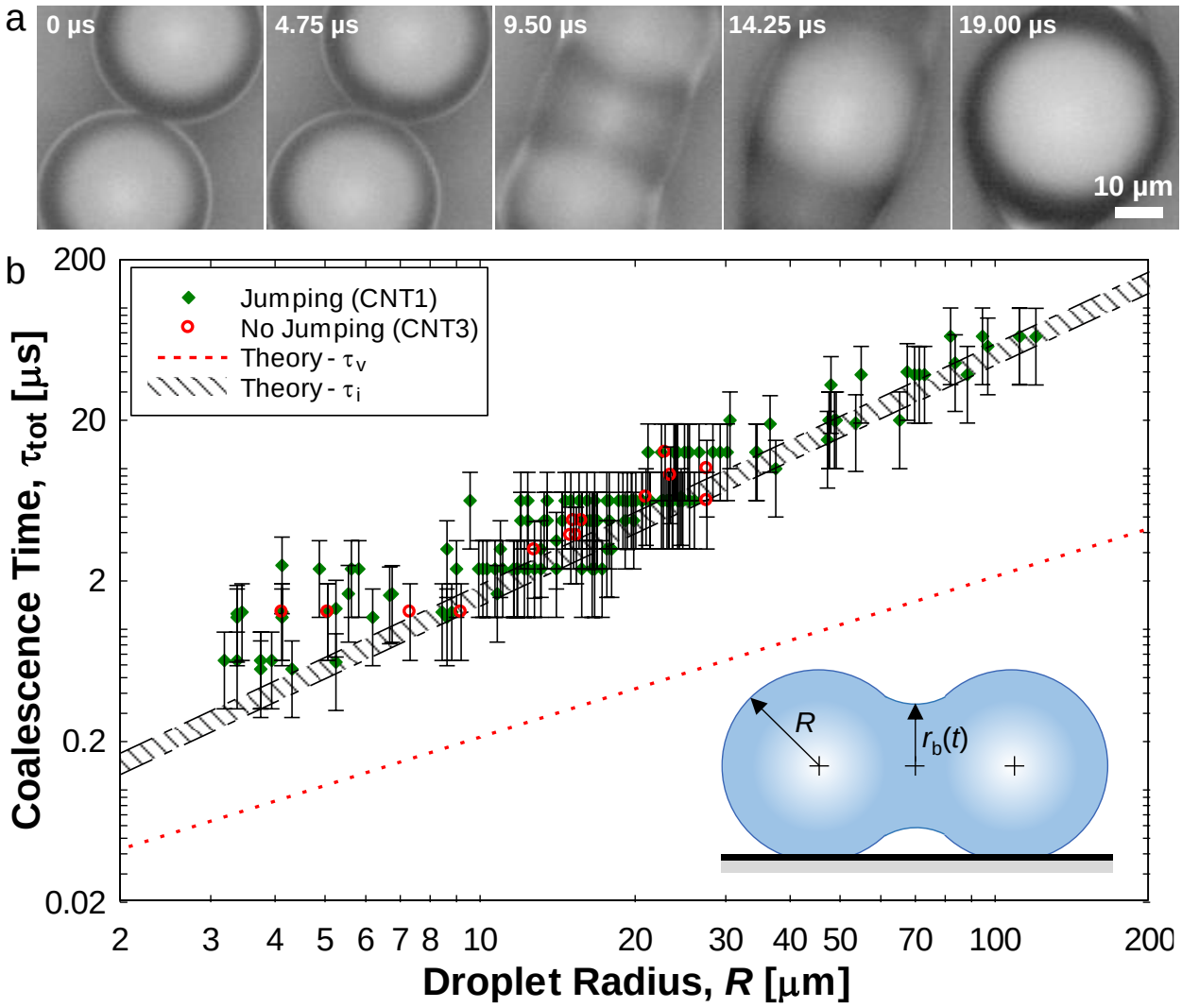

Figure 3. (a) High-speed time-lapse images capturing the coalescence process of two identical (R_1 = 18.5 ± 0.3 µm (bottom) and R_2 = 18.5 ± 0.3 µm (top)) water droplets via top-view optical microscopy. Droplet were formed by condensing water vapor from the ambient air. Experimental conditions: stage and CNT sample temperature T_w = 1 ± 0.5°C, ambient air temperature T_{air} = 22 ± 0.5°C, vapor temperature $T_v = T_{sat}\left(\Phi P_{sat}(T_{air})\right)$ = 2.5 ± 0.5°C, relative humidity Φ = 28 ± 1%, and supersaturation $S = [\Phi P_{sat}(T_{air})]/P_{sat}(T_w)$ = 1.02 ± 0.035. High speed imaging was done at 210,526 frames/s, with an exposure time of 4.75 µs, and a period of 4.396 µs. (b) Two droplet coalescence time (τ_{tot}) as a function of initial droplet radius, R. The coalescence time is defined as the time taken for the bridge radius to reach the droplet radius ($r_b = R$). The filled green diamond and hollow red circle symbols represent experimentally observed jumping events on CNT1 and coalescence without jumping on CNT3, respectively. For inertial-capillary dominated coalescence: $\tau_{tot} = (\rho R^3/\gamma {D_0}^4)^{1/2}$. The shaded region represent the solution for $1.39 < D_0 < 1.62$. For inertially-limited viscous coalescence: $\tau_{tot} = R\mu/\gamma$. The error bars for the measured radii are smaller than the symbol size and are not shown.

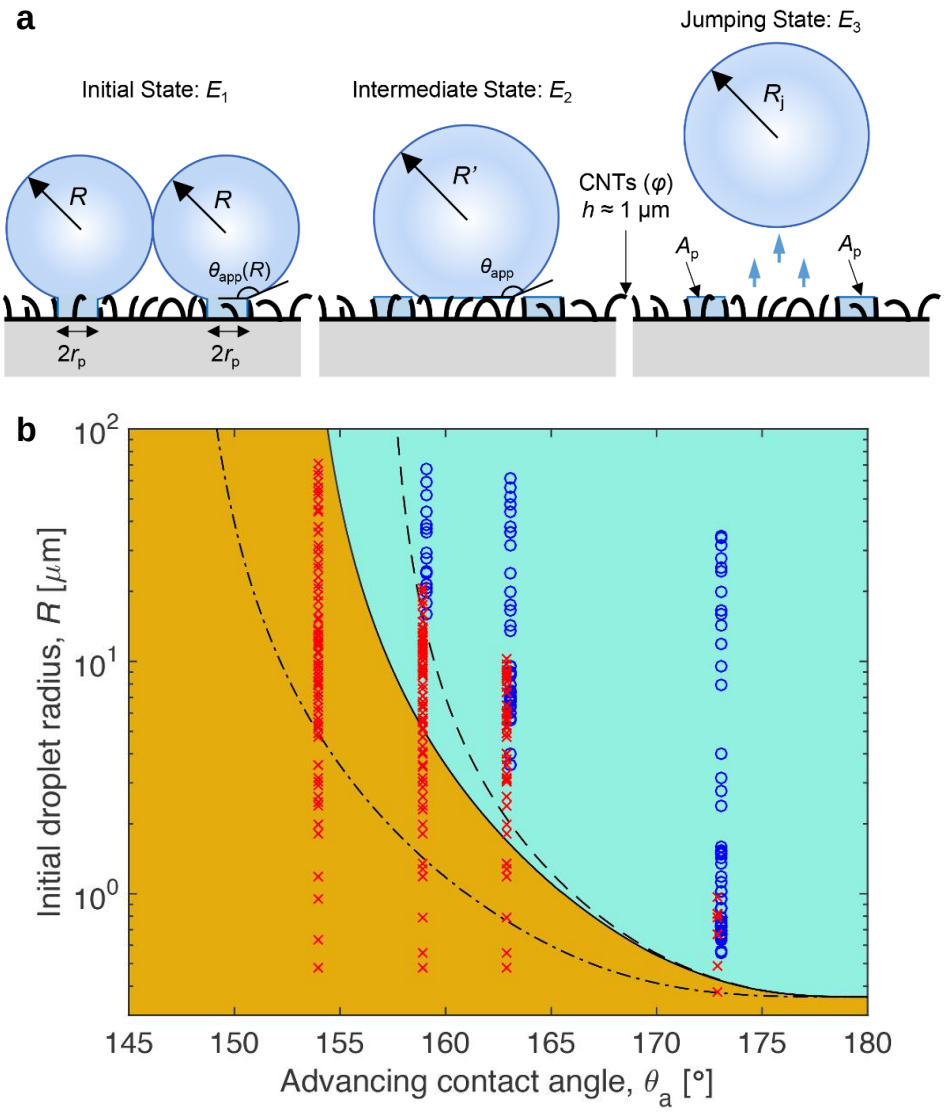

Figure 4. (a) Schematic of droplets residing in state 1 (E_1) just prior to jumping, state 2 (E_2) after coalescing but before departing, and state 3 (E_3) immediately after jumping. (b) Regime map of droplet jumping showing the initial droplet radius (R) as a function of advancing contact angle. The blue circle and red cross symbols represent experimentally observed jumping events and coalescence without jumping, respectively. The solid curve gives the model prediction with hysteresis considering the equilibrium interfacial areas (see a) with r_p = 100 nm. The shaded aquamarine region represents the regime where droplet jumping is allowable ($E_j < 0$), while the shaded orange region represents the regime where droplet jumping does not occur ($E_j > 0$). For comparison, we plot the no hysteresis limit (dot-dash curve). Also shown (dashed curve) is the prediction of the hysteresis model including an additional Oh-dependent adhesion term W' (c = 0.11) accounting for the dynamically wetted area between states E_2 and E_3. Note, the experimental data points are offset to the left and right, respectively, for the CNT1, CNT2, and CNT3 samples to more clearly show the data. Experimental conditions: S = 8.56 ± 0.4, T_w = 1 ± 0.5°C.

CHAPTER 3: CONCLUSIONS

In summary, we demonstrate for the first time the coalescence-induced jumping of coalescing water nanodroplets on superhydrophobic surfaces. The surprisingly small droplet jumping radii we observe reinforces a picture where droplet jumping is governed by capillary-inertial dynamics and fundamentally limited by viscous effects. However, we also demonstrate that, in considering real surfaces, the combined effects of adhesion, contact angle hysteresis and initial wetting behavior governed by the surface structure morphology and length-scale play a defining role. Indeed, it is the coupling of both hydrodynamic and wetting mechanisms that ultimately govern both the minimum droplet jumping size on any given superhydrophobic surface and the reduction in jumping speed at low droplet radii. This work provides key, previously undefined, insights towards designing optimal superhydrophobic structured surfaces for high performance energy and water applications.

REFERENCES

[1] L. Perez-Lombard, J. Ortiz, and C. Pout, Energ Buildings **40**, 394 (2008).

[2] T. B. Peters *et al.*, Ieee T Comp Pack Man **2**, 1637 (2012).

[3] A. D. Khawaji, I. K. Kutubkhanah, and J. M. Wie, Desalination **221**, 47 (2008).

[4] J. M. Beer, Prog Energ Combust **33**, 107 (2007).

[5] A. Bürkholz, *Droplet separation* (VCH Verlagsgesellschaft; VCH Publishers, Weinheim (Federal Republic of Germany), New York, NY (USA), 1989).

[6] E. Schmidt, W. Schurig, and W. Sellschopp, Forsch. Ingenieurwes **1**, 53 (1930).

[7] E. J. Le Fevre and J. W. Rose, in *Proceedings of the Third International Heat Transfer Conference* (ASME, Chicago, IL, 1966), pp. 362.

[8] J. B. Boreyko and C. H. Chen, Phys Rev Lett **103**, 184501 (2009).

[9] R. Enright, N. Miljkovic, J. Sprittles, K. Nolan, R. Mitchell, and E. N. Wang, ACS Nano **8**, 10352 (2014).

[10] F. J. Liu, G. Ghigliotti, J. J. Feng, and C. H. Chen, J Fluid Mech **752**, 39 (2014).

[11] F. J. Liu, G. Ghigliotti, J. J. Feng, and C. H. Chen, J Fluid Mech **752**, 22 (2014).

[12] Y. Nam, H. Kim, and S. Shin, Appl Phys Lett **103** (2013).

[13] Y. Nam, D. Seo, C. Lee, and S. Shin, Soft Matter **11**, 154 (2015).

[14] X. Chen, J. Wu, R. Ma, M. Hua, N. Koratkar, S. Yao, and Z. Wang, Advanced Functional Materials **21**, 4617 (2011).

[15] J. Feng, Y. Pang, Z. Qin, R. Ma, and S. Yao, ACS Applied Materials & Interfaces **4**, 6618−6625 (2012).

[16] J. Feng, Z. Q. Qin, and S. H. Yao, Langmuir **28**, 6067 (2012).

[17] C. J. Lv, P. F. Hao, Z. H. Yao, Y. Song, X. W. Zhang, and F. He, Appl Phys Lett **103**, 021601 (2013).

[18] K. Rykaczewski, Langmuir **28**, 7720 (2012).

[19] K. Rykaczewski, W. A. Osborn, J. Chinn, M. L. Walker, J. H. J. Scott, W. Jones, C. L. Hao, S. H. Yao, and Z. K. Wang, Soft Matter **8**, 8786 (2012).

[20] J. Tian, J. Zhu, H.-Y. Guo, J. Li, X.-Q. Feng, and X. Gao, The Journal of Physical Chemistry Letters **5**, 2084 (2014).

[21] M. McCarthy, K. Gerasopoulos, S. C. Maroo, and A. J. Hart, Nanoscale and Microscale Thermophysical Engineering **18**, 288 (2014).

[22] G. Li, M. H. Alhosani, S. Yuan, H. Liu, A. A. Ghaferi, and T. Zhang, Langmuir **30**, 14498 (2014).

[23] K. Yanagisawa, M. Sakai, T. Isobe, S. Matsushita, and A. Nakajima, Applied Surface Science **315**, 212 (2014).

[24] C.-W. Lo, C.-C. Wang, and M.-C. Lu, ACS Applied Materials & Interfaces **6**, 14353 (2014).

[25] K. M. Wisdom, J. A. Watson, X. Qua, F. Liua, G. S. Watson, and C. H. Chen, Proceedings of the National Academy of Sciences of the United States of America **110**, 7992 (2013).

[26] G. S. Watson, L. Schwarzkopf, B. W. Cribb, S. Myhra, M. Gellender, and J. A. Watson, J R Soc Interface **12** (2015).

[27] G. S. Watson, M. Gellender, and J. A. Watson, Biofouling **30**, 427 (2014).

[28] J. B. Boreyko, Y. J. Zhao, and C. H. Chen, Appl Phys Lett **99**, 234105 (2011).

[29] Q. L. Zhang, M. He, J. Chen, J. J. Wang, Y. L. Song, and L. Jiang, Chem Commun **49**, 4516 (2013).

[30] X. M. Chen, R. Y. Ma, H. B. Zhou, X. F. Zhou, L. F. Che, S. H. Yao, and Z. K. Wang, Sci Rep-Uk **3** (2013).

[31] J. B. Boreyko and P. C. Collier, Acs Nano **7**, 1618 (2013).

[32] J. Y. Lv, Y. L. Song, L. Jiang, and J. J. Wang, ACS Nano **8**, 3152 (2014).

[33] J. B. Boreyko and C. H. Chen, International Journal of Heat and Mass Transfer **61**, 409 (2013).

[34] D. J. Preston, N. Miljkovic, R. Enright, and E. N. Wang, J Heat Trans-T Asme **136** (2014).

[35] N. Miljkovic, D. J. Preston, R. Enright, and E. N. Wang, Nature Communications **4**, 2517 (2013).

[36] N. Miljkovic, D. J. Preston, R. Enright, and E. N. Wang, Appl Phys Lett **105** (2014).

[37] K. G. Zhang, F. J. Liu, A. J. Williams, X. P. Qu, J. J. Feng, and C. H. Chen, Phys Rev Lett **115** (2015).

[38] R. Enright, N. Miljkovic, J. L. Alvarado, K. Kim, and J. W. Rose, Nanosc Microsc Therm **18**, 223 (2014).

[39] N. Miljkovic and E. N. Wang, Mrs Bull **38**, 397 (2013).

[40] R. Enright, N. Miljkovic, N. Dou, Y. Nam, and E. N. Wang, J Heat Transf **135**, 091304 (2013).

[41] N. Miljkovic, R. Enright, and E. N. Wang, ACS Nano **6**, 1776 (2012).

[42] N. Miljkovic, R. Enright, and E. N. Wang, 3rd Micro/Nanoscale Heat & Mass Transfer International Conference (2012).

[43] N. Miljkovic, R. Enright, and E. N. Wang, J Heat Transf **135** (2013).

[44] J. Cheng, A. Vandadi, and C. L. Chen, Appl Phys Lett **101**, 131909 (2012).

[45] E. Olceroglu, C. Y. Hsieh, M. M. Rahman, K. K. S. Lau, and M. McCarthy, Langmuir **30**, 7556 (2014).

[46] E. Olceroglu, S. M. King, M. M. Rahman, and M. McCarthy, Proceedings of the Asme International Mechanical Engineering Congress and Exposition - 2012, Vol 7, Pts a-D, 2809 (2013).

[47] D. Attinger, C. Frankiewicz, A. R. Betz, T. M. Schutzius, R. Ganguly, A. Das, C.-J. Kim, and C. M. Megaridis, MRS Energy & Sustainability **1** (2014).

[48] X. M. Chen, J. A. Weibel, and S. V. Garimella, Adv Mater Interfaces **2** (2015).

[49] Y. M. Hou, M. Yu, X. M. Chen, Z. K. Wang, and S. H. Yao, ACS Nano **9**, 71 (2015).

[50] N. Miljkovic, R. Enright, Y. Nam, K. Lopez, N. Dou, J. Sack, and E. N. Wang, Nano Lett **13**, 179 (2013).

[51] P. Birbarah, Z. E. Li, A. Pauls, and N. Miljkovic, Langmuir **31**, 7885 (2015).

[52] T. Q. Liu, W. Sun, X. Y. Sun, and H. R. Ai, Colloid Surface A **414**, 366 (2012).

[53] C. J. Lv, P. F. Hao, Z. H. Yao, and F. L. Niu, Langmuir **31**, 2414 (2015).

[54] F. C. Wang, F. Q. Yang, and Y. P. Zhao, Appl Phys Lett **98** (2011).

[55] X. L. Liu and P. Cheng, Int Commun Heat Mass **64**, 7 (2015).

[56] X. L. Liu, P. Cheng, and X. J. Quan, Int J Heat Mass Tran **73**, 195 (2014).

[57] B. L. Peng, S. F. Wang, Z. Lan, W. Xu, R. F. Wen, and X. H. Ma, Appl Phys Lett **102**, 151601 (2013).

[58] R. Enright, N. Miljkovic, A. Al-Obeidi, C. V. Thompson, and E. N. Wang, Langmuir **28**, 14424 (2012).

[59] D. Kaschiev, *Nucleation: Basic Theory With Applications* (Butterworth Heinemann, Oxford, 2000).

[60] J. D. Paulsen, J. C. Burton, and S. R. Nagel, Phys Rev Lett **106**, 114501 (2011).

[61] J. D. Paulsen, J. C. Burton, S. R. Nagel, S. Appathurai, M. T. Harris, and O. A. Basaran, Proceedings of the National Academy of Sciences of the United States of America **109**, 6857 (2012).

[62] S. T. Thoroddsen, K. Takehara, and T. G. Etoh, J Fluid Mech **527**, 85 (2005).

[63] M. M. Wu, T. Cubaud, and C. M. Ho, Phys Fluids **16**, L51 (2004).

[64] Z. Liang and P. Keblinski, Appl Phys Lett **107** (2015).

[65] M. He *et al.*, Soft Matter **8**, 6680 (2012).

[66] M.-K. Kim, H. Cha, P. Birbarah, S. Chavan, C. Zhong, Y. Xu, and N. Miljkovic, Langmuir **31**, 13452 (2015).

[67] K. Rykaczewski, J. H. J. Scott, and A. G. Fedorov, Appl Phys Lett **98**, 093106 (2011).

[68] M. Kollera and U. Grigull, Wärme - und Stoffübertragung **2**, 31.

[69] M. M. Wu, T. Cubaud, and C. M. Ho, Phys Fluids **16**, 51 (2004).

[70] S. Farokhirad, J. F. Morris, and T. Lee, Phys Fluids **27**, 102102 (2015).

[71] Y. Cheng, J. Xu, and Y. Sui, International Journal of Heat and Mass Transfer **95**, 506 (2016).

APPENDIX A: EXPERIMENTAL SETUP AND PROCEDURES

Droplet coalescence, jumping, and distribution behavior were studied using a custom built top-view optical light microscopy set-up shown diagrammatically in Fig. A1, and substantially similar to the one described in Ref. [66]. Samples were horizontally mounted using a thin layer of thermal grease (Omegatherm, Omega, thermal conductivity of 2.2 W/m·K) to a cold stage (Instec, TP104SC-mK2000A) and cooled to the test temperature of T_{w} = 1 ± 0.5°C, in a laboratory environment having air temperature, T_{air} = 22 ± 0.5°C, and relative humidity (RH), Φ = 28 ± 1% (Roscid Technologies, RO120). The RH of the laboratory air could vary up to ± 10% over the course of a day. To ensure stable humidity conditions, the ambient condition experiments were conducted in hour-long segments when the laboratory air RH reached 28%, and ended when the RH exceeded 30% or fell below 26%.

A supply of water-saturated N2 was obtained by sparging a temperature controlled stainless-steel water reservoir with dry N2. A reservoir by-pass valve was installed to provide dry N2 to the sample as it was being cooled to the set point temperature at the beginning of each experiment, T_{w} = 1 ± 0.5°C. Once the stage temperature stabilized to the test temperature, the by-pass valve was closed to initiate the flow of water-saturated N2 to the sample enclosure at a constant flow rate of $Q \approx$ 2.5 L/min, marking the start of the experiment. The humidity (Roscid Technologies, RO120) was recorded throughout the experiment. The supersaturation was controlled by adjusting the water reservoir temperature through which the N2 was sparged. Experiments were run at two vapor conditions: (1) ambient conditions (no supply vapor flow) corresponding to T_{air} = 22 ± 0.5°C, T_{w} = 1 ± 0.5°C, relative humidity Φ = 28 ± 1%, supersaturation $S = [\Phi P_{\mathrm{sat}}(T_{\mathrm{air}})]/P_{\mathrm{sat}}(T_{\mathrm{w}})$ = 1.02 ± 0.035, and nucleation density $N \leq$ 2.5 x 109 droplets/m2, and (2) breath figure conditions

corresponding to T_{air} = 35 ± 0.5°C, T_w = 1 ± 0.5°C, $\Phi \approx 100 \pm 1\%$, S = 8.56 ± 0.4, and $N \geq$ 1.1 x 1010. The second condition (breath figure) was chosen due to our availability to check the conditions by blowing through a 0.5" diameter silicone tube on to the sample, and observing identical condensation conditions as the vapor supply case. Exhaled human breath is composed of CO2 and saturated water vapor at ≈ 36°C.

Video recordings were performed at variable frame rates (up to 600,000 frames-per-second) with a high speed camera (Phantom, V711, Vision Research) attached to an upright microscope (Eclipse LV100, Nikon). Droplet nucleation, growth, and departure were recorded at variable time intervals using the high speed camera, operating at variable resolutions ranging from 1280 x 800 to 60 x 40 pixels depending on the exposure time and recoding speed. Imaging was performed with either a 20X (TU Plan Fluor EPI ELWD, Nikon), 50X (TU Plan Fluor EPI ELWD, Nikon), or 100X (TU Plan Fluor EPI ELWD, Nikon) objective (Lens 1 in Fig. A1). Extra-long working distance (ELWD) lenses were used in order to maximize the distance from the top of the sample to the lens tip, and avoid interference between the optics and jumping droplets. For the 50X and 100X lenses, the working distance was measured to be 11 and 4 ± 0.5 mm, respectively. Prior to experimentation, the size per pixel was calibrated by observing a 10 μm diameter deep reactive ion etched pillar sample at full resolution and at each magnification (50X and 100X). Prior to optical microscopy, the size of the pillars was known and determined with field emission scanning electron microscopy (S-4800, Hitachi), allowing us to back calculate the minimum size per pixel at 0.075 μm/pixel at the 100X magnification.

Illumination was supplied by an LED light source (SOLA SM II Light Engine, Lumencor). The

LED light source was specifically chosen for its high-intensity, low power consumption (2.5 W), and narrow spectral range (380 - 680 nm), in order to minimize heat generation at the surface due to light absorption. Furthermore, by manually reducing the condenser aperture diaphragm opening size and increasing the camera exposure time, we were able to minimize the amount of light energy needed for illumination and hence minimize local heating effects during condensation experiments.[67]

A.1. Figures

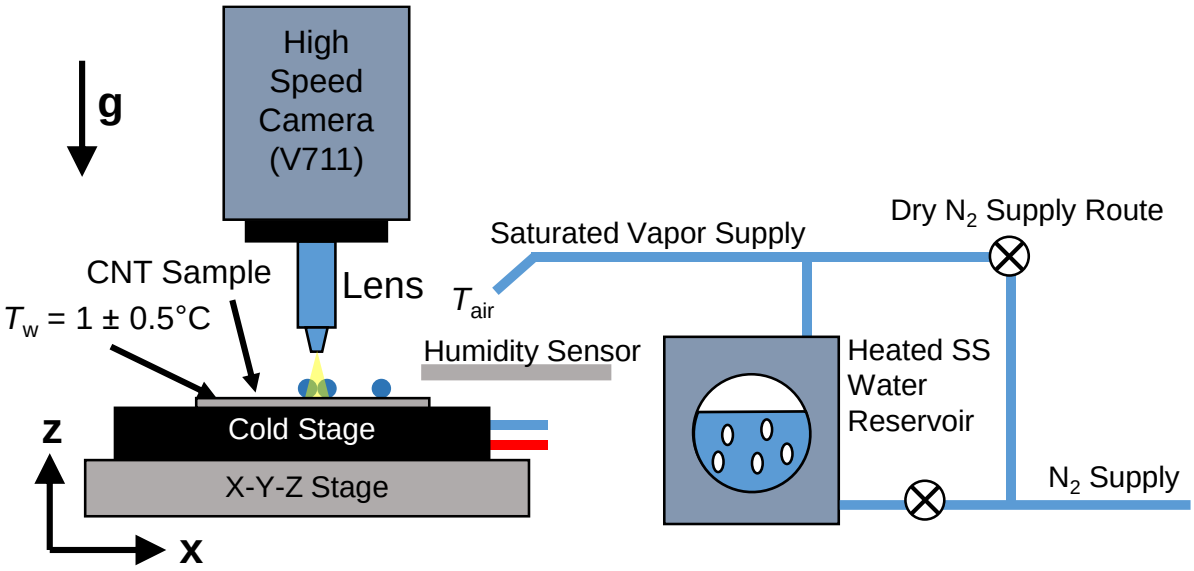

Figure A1. Schematic of the top-view microscopy experimental setup. To control the supersaturation, a heated reservoir was used to supply water vapor. Air and sample temperatures were measured with external K-type thermocouples, and internal built in thermocouples inside the cold stage apparatus. Schematic not to scale.

APPENDIX B: DROPLET-SURFACE INTERACTION MODEL

To estimate the excess surface energy required to overcome the work of adhesion associated with finite surface adhesion, we developed an analytical model that considers the coalescence of two droplets having center-to-center spacing $2R$, with partially pinned liquid regions underneath each droplet characterized by a radius, r_{p}. No jumping will occur if the available excess liquid/vapor surface energy released during coalescence is unable to overcome the work of adhesion associated with the finite wetted area of the droplets on the surface. The work of adhesion is considered to play a role throughout the coalescence process, from the initial stage of bridge formation (identified as stage 1 & 2 by Liu et al. [10]) to the acceleration of the droplet mass perpendicular to the surface (identified as stage 3 by Liu et al. [10]). Recent 3D simulations of the coalescence process on surfaces with $\theta < 180°$ provide information regarding the characteristic surface wetting behavior of jumping droplets at the different stages of coalescence.[13] To develop our model incorporating the role of surface adhesion on droplet jumping within a simple energy balance framework, we divide the jumping process into three states rather than the two states typically considered.[17,53,54,68] Specifically, besides the initial state before coalescence (E_1) and the final jumping state (E_3), we consider an intermediate state representing the coalesced droplet on the surface prior to departure (E_2). Note that this intermediate state (E_2) is a well-defined equilibrium state if jumping does not occur.

The excess liquid-vapor interfacial energy driving the jumping process, $\Delta E_{31,lv}$, is calculated between the initial (E_1) and final energy state (E_3), albeit corrected by an efficiency term, η, that captures the characteristic incomplete conversion of excess liquid-vapor interface energy to the translational kinetic energy of the jumping droplet and viscous effects.[9,10] Furthermore, we also

consider the difference in the work of adhesion between E_1 and E_2, $W_{31} - W_{32}$, where W_{32} is characteristically smaller than W_{31}. We consider this adhesion term balancing directly against the **total** excess energy, since the work of adhesion to be overcome is acting against droplet mass moving parallel to the surface as the radial flow, characteristic of the coalescence process, begins to develop. Finally, in order to transition from E_2 to E_3, the droplet needs to overcome the work of adhesion associated with the droplet base area in state E_2 (W_{32}), and balances directly against the **available** excess energy for jumping. Thus, in the ideal limit of zero contact angle hysteresis, we estimate the energy available for jumping as

$$E_{\mathrm{j}} \approx \eta\left[\Delta E_{31,\mathrm{lv}} + (W_{31} - W_{32})\right] + W_{32}\,, \tag{B1}$$

where the excess liquid-vapor interface energy between state E3 and E1 is given by

$$\Delta E_{31,\mathrm{lv}} = \gamma_{\mathrm{lv}}\left(A_{3,\mathrm{lv}} - A_{1,\mathrm{lv}}\right), \tag{B2}$$

the work of adhesion associated with E1 is

$$W_{31} = \gamma_{\mathrm{lv}}(1 + \cos\theta)A_{1,\mathrm{ls}}\,, \tag{B3}$$

the work of adhesion associated with E2 is

$$W_{32} = \gamma_{\mathrm{lv}}(1 + \cos\theta)A_{2,\mathrm{ls}}\,, \tag{B4}$$

where γ_{lv} is the liquid vapor interfacial tension (≈75 mN/m), $A_{1,\mathrm{lv}}$ is the liquid/vapor area in E_1, $A_{3,\mathrm{lv}}$ is the liquid/vapor area in E_3, $A_{1,\mathrm{ls}}$ is the liquid/solid area in E_1 and $A_{2,\mathrm{ls}}$ is the liquid/surface area in E_2. It is important to note, all energies are calculated as the difference between final/intermediate state (E_3, E_2) and initial state (E_1). Thus, excess liquid/vapor energy is a negative quantity, adhesion is a positive quantity and the jumping speed is $v_j = \sqrt{-2E_{\mathrm{j}}/\rho V}$. The initial liquid/vapor and liquid/solid interface areas are given, respectively, by

$$A_{1,\mathrm{lv}} = 4\pi R^2(1 - \cos\theta) \tag{B5}$$

and

$$A_{1,\mathrm{ls}} = 2\pi R^2 \sin^2\theta. \tag{B6}$$

The other relevant interfacial areas are determined by first considering the total conserved volume of the system based on the two initial droplets of radius R and contact angle θ given by

$$V = \frac{2\pi R^3}{3}(\cos\theta - 1)^2(\cos\theta + 2). \tag{B7}$$

so that the intermediate droplet radius (E_2) is

$$R' = \sqrt[3]{\frac{3V}{\pi(\cos\theta - 1)^2(\cos\theta + 2)}}\,, \tag{B8}$$

the liquid/vapor and liquid/solid interfacial areas are, respectively,

$$A_{2,\mathrm{lv}} = 2\pi R'^2(1 - \cos\theta)\,, \tag{B9}$$

and

$$A_{2,\mathrm{ls}} = \pi R'^2 \sin^2\theta. \tag{B10}$$

The jumping droplet radius (E_3) is similarly given by considering Eq. B8 as

$$R_{\mathrm{j}} = \sqrt[3]{\frac{3V}{4\pi}}, \tag{B11}$$

and the jumping droplet liquid/vapor interfacial area is

$$A_{3,\mathrm{lv}} = 4\pi R_{\mathrm{j}}^2. \tag{B12}$$

It should be noted that we recover the typical two-state expression for the available jumping energy by setting η = 1.[17,53,54,68] The efficiency term in Eq. B1 is obtained from the analysis of Enright et al.[9] Here we implicitly assume that the useful internal flow momentum generated during coalescence scales proportionally with the perturbation to the droplet excess surface energy when θ < 180°, which is reasonable when the departure from 180° is small. Note, however, that

our previous analysis and resulting expression for η was only valid for Ohnesorge numbers Oh (= $\mu/(\rho\gamma_{\mathrm{lv}}R)^{1/2}) \leq 0.12$ in the small Bond number limit, Bo (= $\rho g R^2/\gamma_{\mathrm{lv}}$) → 0

$$\eta = (3.4026\mathrm{Oh}^2 - 1.5285\mathrm{Oh} + 0.2831)^2\left[3\left(2 - 2^{2/3}\right)\right]^{-1} \quad \text{for } \mathrm{Oh} \leq 0.12. \tag{B13}$$

In order to define the efficiency for Oh > 0.12, we assume an exponentially decaying efficiency due to the increasing role of viscous dissipation at large Oh. Such behavior is physically reasonable considering the viscous dissipation behavior observed in our previous simulations,[9] but suffers from the fact that the efficiency defined by a simple exponential decay function never goes to zero at a cut-off Oh, $\mathrm{Oh_c}$. The $\mathrm{Oh_c}$ corresponds to the droplet size where the viscous-to-inertial cross-over bridge radius, r_c, is equal to the droplet radius, R, and is found from the definition of the cross-over timescale and bridge radius scaling [60]

$$\mathrm{Oh_c} = D_0^2/8 \tag{B14}$$

where D_0 is a constant whose value ranges between 1.39 and 1.62.[60,62,69] This expression provides an upper bound on Oh where droplet jumping is possible by finding the droplet size where the bridging flow during coalescence is completely viscously damped. Taking D_0 = 1.62, (B14) predicts $\mathrm{Oh_c} \approx 0.33$. Plotting the critical initial droplet radius, $R(\mathrm{Oh_c})$, as a function of temperature, we observe that $R(\mathrm{Oh_c})$ decreases from ~ 400 nm at 0 °C to ~ 130 nm at 20 °C.

To capture $\mathrm{Oh_c}$ in our model, we define a double exponential expression

$$\eta = a\left[e^{-\mathrm{bOh}} - \left(1 - e^{-\mathrm{bOh}}\right)e^{-\mathrm{bOh_c}}\right], \tag{B15}$$

where the coefficient a gives the maximum efficiency as Oh → 0 in the limit of small Bo and the term in the brackets approximates the viscous effect as a function of Oh. Figure B2 shows the results of the fit of (B15) with $\mathrm{Oh_c} \approx 0.33$ to our previous numerical data.[9]

In Figure B3, we compare the 3D simulation results of Liu et al.[10] to our efficiency expression, (B15) using the fit parameters given in Figure B2, evaluated in terms of the scaled jumping speed

as

$$\frac{v_j}{U} = \sqrt{\eta 3(2 - 2^{2/3})}\,, \tag{B16}$$

where $U = \sqrt{\gamma_{lv}/\rho R}$ is the inertial-capillary scaling of the jumping speed.[8] We find good agreement with the full 3D simulation results, importantly capturing the steep reduction in the scaled jumping speed as the jumping droplet radius reduces below ≈ 2 μm.

In the limit of no contact angle hysteresis, we can generate a phase map for jumping as a function of contact angle and Oh. The phase map shows that jumping is not possible for $\theta \lesssim 150°$ for small Oh. We also observe that the critical contact angle for jumping increases as Oh increases up to the no adhesion limit (θ = 180°) where E_j = 0 at Oh = $\mathrm{Oh_c}$. The model results are in qualitative agreement with recent 3D lattice Boltzmann simulations,[70] showing a very similar envelope where jumping is possible. However, our model suggests a larger critical Oh due to our choice of the cut-off radius. We note that our model suffers from the fact that it cannot implicitly account for external fluid interactions, which have been shown numerically to effectively change $\mathrm{Oh_c}$.[10,70]

To consider the more general case where finite contact angle hysteresis exists, we redefine (B1) as

$$E_\mathrm{j} \approx \eta\left[\Delta E_{31,\mathrm{lv}} + (W_{31} - W_{32})\right] + W_{32} + W'. \tag{B17}$$

To account for the additional adhesion associated with the pinned regions beneath the droplets, we assume that complete dewetting of the liquid from the structured region is energetically unfavorable compared to some portion of the liquid remaining pinned within the structures on the surface. Thus, the work of adhesion associated with E_1 is redefined as

$$W_{31} = \gamma_\mathrm{lv}\left[\left(1 + \cos\theta_\mathrm{r}^\mathrm{app}\right)\left(A_{1,\mathrm{ls}} - 2A_\mathrm{p}\right) + [(2 - \varphi) + \varphi\cos\theta_\mathrm{r}]2A_\mathrm{p}\right], \tag{B18}$$

where $A_\mathrm{p} = \pi {r_\mathrm{p}}^2$ is the pinned area beneath each droplet, $\theta_\mathrm{r}^\mathrm{app}$ is the apparent receding angle, θ_r is the receding contact angle on a smooth surface coated with the hydrophobic coating (≈112.6°)

and φ is the wetted surface solid fraction associated with the droplet residing in the Cassie-Baxter state. We estimate φ from the advancing apparent contact angle using the Cassie-Baxter equation, $\varphi = \left(\cos\theta_{\mathrm{a}}^{\mathrm{app}} + 1\right)/(\cos\theta_{\mathrm{a}} + 1)$. The first term in the brackets captures the work of adhesion associated with the wetted area of the surface beyond the pinned base region. Within the second term, the first term in the brackets (2 - φ) represents the creation of new liquid vapor interface between the CNT structures and on the departing droplet. The second term ($\varphi \cos\theta_{\mathrm{r}}$) represents the creation of liquid vapor interface on top of the CNT structures due to droplet surface separation from state 1 to 2. The pinned base radius, r_{p}, is associated with the initial growth of the condensed droplet nucleating within the CNT nanostructure[40,58] and has been estimated to be ≈100 nm for CNT1 in our previous study.[9] We do not expect the pinned base radius r_{p} to increase with increasing polymer thickness since the CNT length scale sets this dimension.[58] However, r_{p} might decrease with increasing polymer thickness due to a slight change in initial growth behavior due to increasing solid fraction. [58] Assuming that r_{p} is approximately constant for all of our CNT samples, we can estimate the cross-over to constant contact angle growth at the intersection between the r_{p} dependent contact angle and the macroscopically measured advancing angle. This implies that the switch to constant contact angle growth occurs at smaller droplet radii with decreasing apparent advancing contact angle. Radius-dependent contact angle behavior will continue up to the point where the interface of the droplet makes contact with surrounding nanostructures and begins spreading over the surface in the Cassie state with an approximately constant advancing angle, $\theta_{\mathrm{a}}^{\mathrm{app}}$ ≈ 173°, 163°, 159°, and 154° for the δ = 10, 30, 60, and 90 nm surfaces, respectively. The early stage variation in the apparent advancing contact angle was modeled as:[40,43]

$$\theta_{\mathrm{a}}^{\mathrm{app}}(R) = \cos^{-1}\left(\frac{r_{\mathrm{p}}}{R}\right) + \frac{\pi}{2}. \tag{B19}$$

The droplet cross-over radius is found by substituting the macroscopic apparent advancing contact angle into (B19) and solving for R to give

$$R_{\mathrm{C}} = \frac{r_{\mathrm{p}}}{\cos\left(\theta_{\mathrm{a,macro}}^{\mathrm{app}} - \frac{\pi}{2}\right)}. \tag{B20}$$

In Figure B5, we plot the model behaviour of the apparent advancing contact angle for our four CNT surfaces. All surfaces are expected to reach constant contact angle growth mode before their radius reaches 1 μm due to the small pinned base radius.

To define the contact angle hysteresis specific to the type of surfaces studied here, we fit an expression to the measured contact angle hysteresis as shown in Fig. B6. We plot our experimental $\Delta\cos\theta^{\mathrm{app}} = \cos\theta_{\mathrm{r}}^{\mathrm{app}} - \cos\theta_{\mathrm{a}}^{\mathrm{app}}$ as a function of $1 + \cos\theta_{\mathrm{a}}^{\mathrm{app}}$ and fit to the data to

$$\Delta\cos\theta^{\mathrm{app}} = m\left(1 + \cos\theta_{\mathrm{a}}^{\mathrm{app}}\right)^{n} \tag{S21}$$

The work of adhesion associated with E_2 is re-defined as

$$W_{32} = \gamma_{\mathrm{lv}}\left(1 + \cos\theta_{\mathrm{r}}^{\mathrm{app}}\right)A\left(\theta_{\mathrm{a}}^{\mathrm{app}}\right)_{2,\mathrm{ls}}, \tag{S22}$$

where the wetted area in E_2 is defined by the macroscopic apparent advancing angle. The additional work of adhesion term in (B17),

$$W' = \gamma_{\mathrm{lv}}\left(\cos\theta_{\mathrm{r}}^{\mathrm{app}} - \cos\theta_{\mathrm{a}}^{\mathrm{app}}\right)A'_{2,\mathrm{ls}}, \tag{S23}$$

is defined to capture the additional surface area wetted during the bridge impact process that plays a role in the overall adhesion of the droplet to the surface when the surface wetting is hysteretic. The additional wetted area, $A'_{2,\mathrm{ls}}$, is generated by the inertia of the bridging flow that forces the contact line beyond its equilibrium advancing position. This peak in wetted surface area has been observed in previous numerical simulations.[12,68] Beyond these observations, little is known quantitatively about this aspect of the coalescence process. Here we consider that the value of $A'_{2,\mathrm{ls}}$

should be a function of both the droplet equilibrium advancing angle and Oh. Indeed, as Oh becomes large and the available inertia to drive this dynamic wetting event decreases, we expect $A'_{2,\mathrm{ls}} \to 0$. Thus, we define

$$A'_{2,\mathrm{ls}} = f A_{2,\mathrm{ls}}\,, \tag{B24}$$

where $f(Oh)$ is a factor dependent functionally on Oh. Since $\eta \propto A$, we expect $f(Oh) \propto \eta$ and define

$$f = c[e^{-bOh} - (1 - e^{-bOh})e^{-bOh_c}], \tag{B25}$$

where c is a constant of proportionality. We note that re-analysis of available numerical data could help clarify this aspect of the coalescence process.[10,12,13,70,71] Table B1 summarizes the details of the surfaces studied and the observed critical jumping radius ($\boldsymbol{R_c}$), below which no jumping was observed.

Table B2 summarizes the results of the calculations using inputs from Table B1, Eq. (B19). We used a value of $\boldsymbol{c}$ = 0.11 in our calculations. The results show excellent agreement with the experimentally observed values of $\boldsymbol{R_c}$.

B.1. Figures

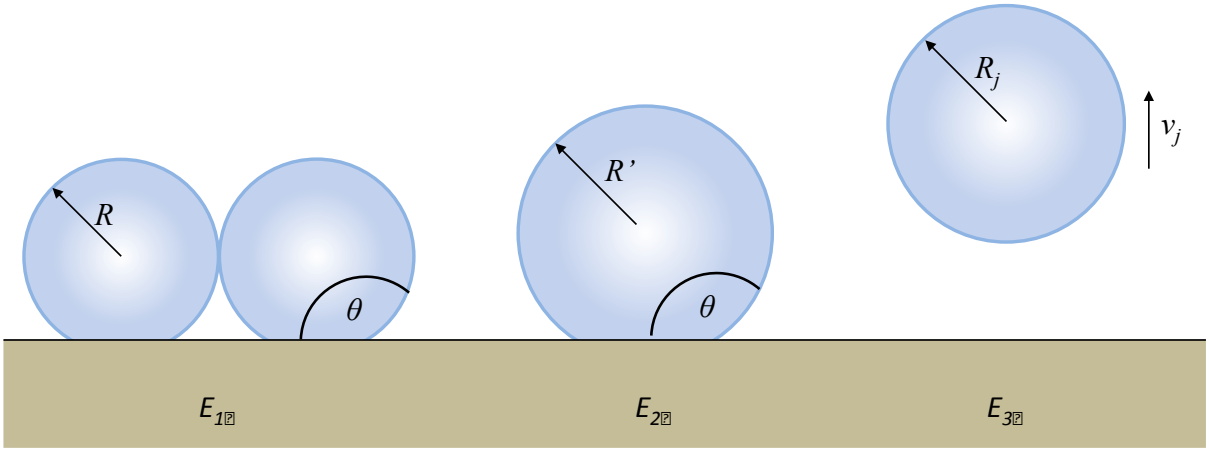

Figure B1. Schematic of droplets residing in state 1 (E_1) just prior to jumping, state 2 (E_2) after coalescing but before departing, and state 3 (E_3) immediately after jumping.

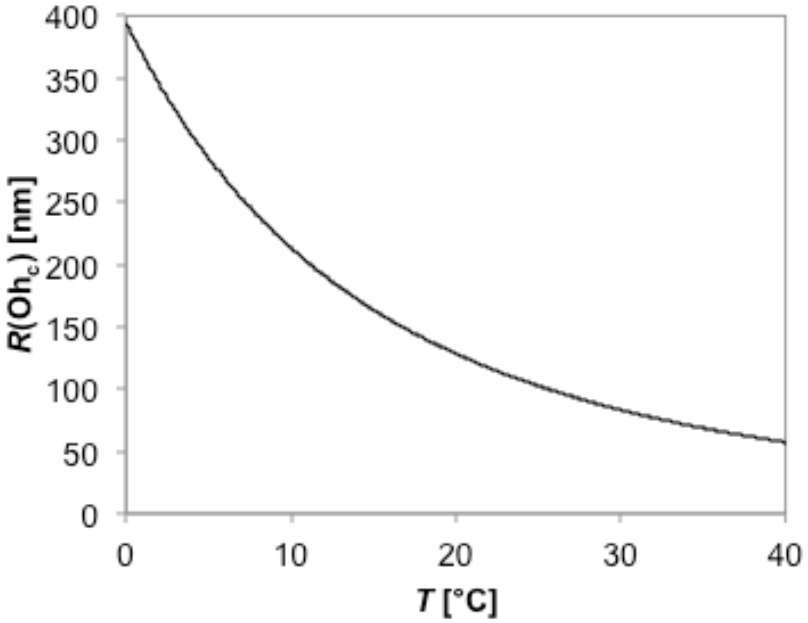

Figure B2. Critical initial droplet radius as a function of droplet temperature with $Oh_c = 0.328$.

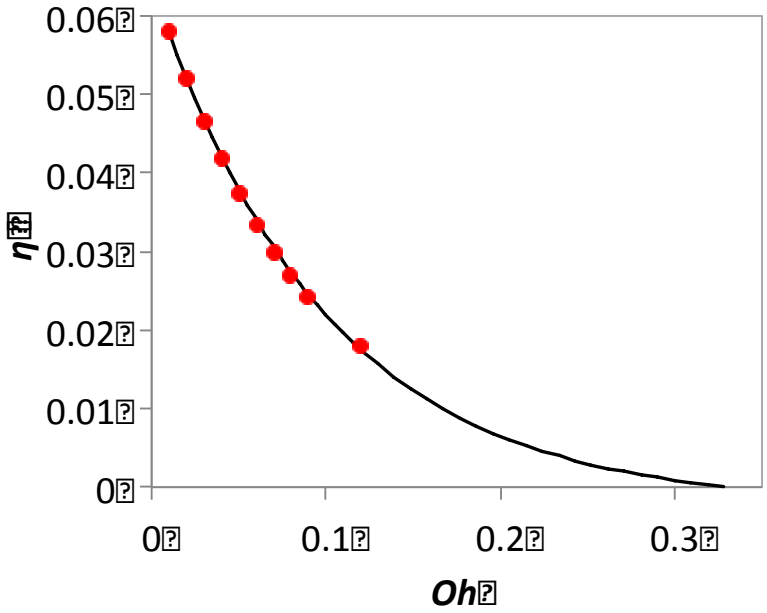

Figure B3. Fit of (B15) to numerical data to obtain η for $0 \leq \mathrm{Oh} \leq \mathrm{Oh_c}$. A best fit of Eq. B15 to the numerical data with $\mathrm{Oh_c} = 0.32805$ gives $a = 0.064362$ and $b = 10.165$. The Pearson product moment of the fit is $R^2 = 0.99948$.

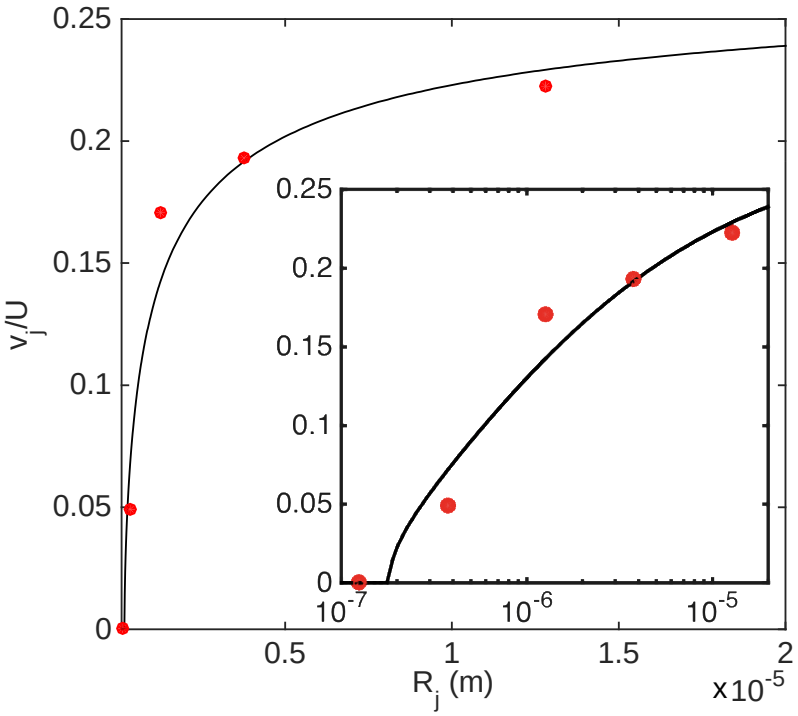

Figure B4. Comparison of the exponentially decaying jumping efficiency expression, (B16, solid curve, to the 3D numerical results of Liu et al.[10] (red circles) in terms of the scaled jumping speed versus droplet jumping radius (R_j). Properties taken from Ref. [10] corresponding to water at 20°C.

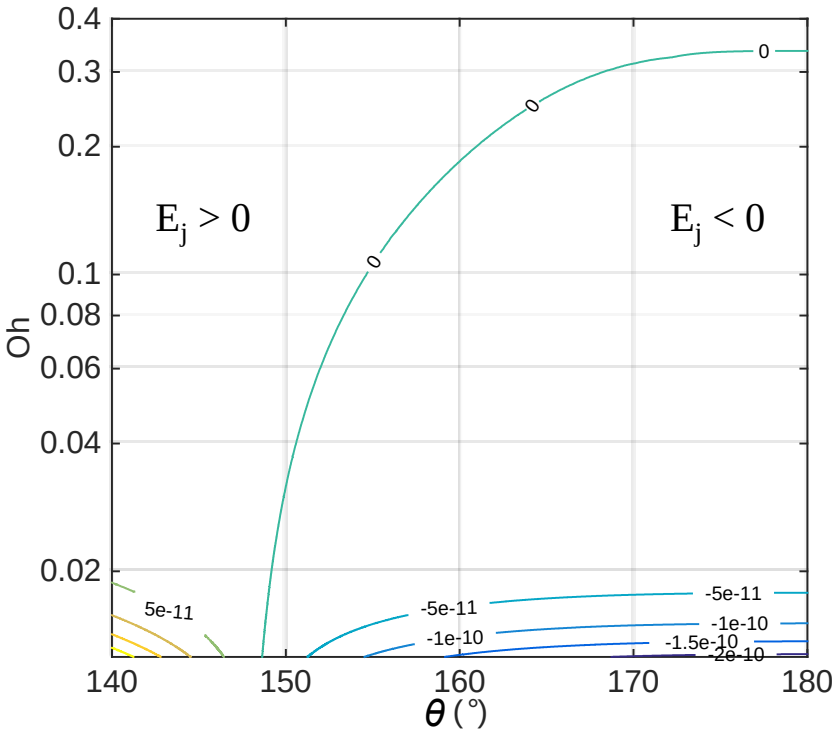

Figure B5. Jumping droplet phase map in terms of Oh and contact angle (θ) for the idealized case where the jumping surface demonstrates zero contact angle hysteresis. In the right-hand side region bounded by the $E_j < 0$ contour, Eq. B1 predicts jumping is possible, while in the left-hand side region bounded by the $E_j > 0$ contour, $E_j > 0$ such that jumping is not possible.

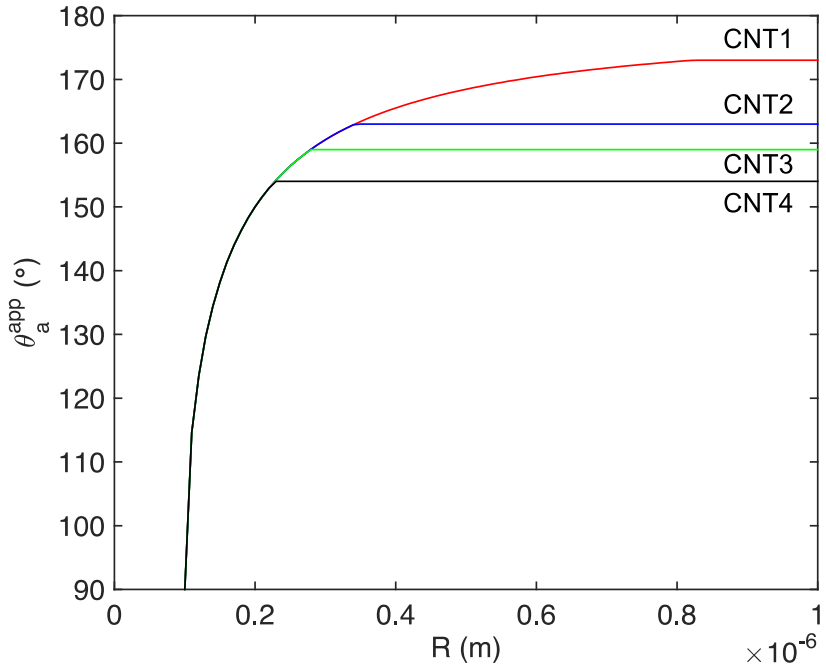

Figure B6. Apparent advancing contact angle model. The apparent contact angle varies with droplet radius given by Eq. (B19) from a pinned base radius of r_p = 100 nm that is assumed constant for the four CNT surfaces. The cross-over to constant contact angle growth occurs when the advancing contact angle equals the macroscopically measured value from Eq. B20.

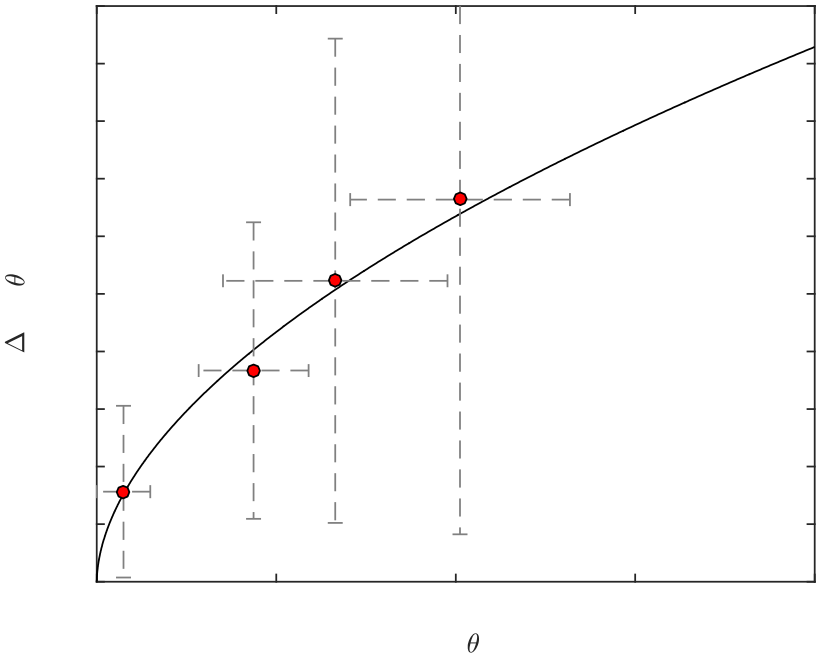

Figure B7. Contact angle hysteresis model. Fit of Eq. (S21) to the experimental contact angle data to obtain contact angle hysteresis for $\theta_a^{app} \leq 180°$. A best fit of Eq. (S21) to the numerical data gives m = 0.4497 and n = 0.5492. The Pearson product moment of the fit is R^2 = 0.9902.

B.2. Tables

Table B1. Surface parameters and measured contact angles and critical jumping radius used in fitting the jumping model with hysteresis.

Sample	t_{P2i}	$\boldsymbol{\theta}_{a,app}$	$\boldsymbol{\theta}_{r,app}$	$\boldsymbol{\varphi}$	$\boldsymbol{R}_c$ (experiment)
P2i	10 nm	124.3	112.6	NA	NA
CNT 1	10nm	173°±3.5°	164°±6°	~0.017	556 nm
CNT 2	30 nm	163°±3°	152°±6°	~0.059	3.57 um
CNT 3	60 nm	159°±5°	146°±8°	~0.152	15.87 um
CNT 4	90 nm	154°±4°	140°±10°	~0.232	Not observed

Table B2. Surface parameters used in fitting the jumping model with hysteresis and calculated critical jumping radius.

Sample	c	$\boldsymbol{\theta}_{a,app}$	$\boldsymbol{\theta}_{r,app}$[i]	$\boldsymbol{\varphi}$	$\boldsymbol{R}_c$ (theory)
CNT 1	0.11	173°	164.1°	~0.017	425 nm
CNT 2	-	163°	151.1°	~0.059	2.05 μm
CNT 3	-	159°	146.3°	~0.152	14.75 μm
CNT 4	-	154°	140.4°	~0.232	No jumping predicted

[i] Based on fit to data, Eq. (S21)